Mechanism of nonlinear flow pattern selection in moderately non-Boussinesq mixed convection

Sergey A. Suslov*
Mathematics, FEIS, Swinburne University of Technology, P.O. Box 218, H38, Hawthorn, Victoria 3122, Australia
(Received 10 September 2009; published 1 February 2010)

Nonlinear (non-Boussinesq) variations in fluid's density, viscosity, and thermal conductivity caused by a large temperature gradient in a flow domain lead to a wide variety of instability phenomena in mixed convection channel flow of a simple gas such as air. It is known that in strongly nonisothermal flows, the instabilities and the resulting flow patterns are caused by competing buoyancy and shear effects [see S. A. Suslov and S. Paolucci, J. Fluid Mech. **302**, 91 (1995)]. However, as is the case in the Boussinesq limit of small temperature gradients, in moderately non-Boussinesq regimes, only a shear instability mechanism is active. Yet in contrast to Boussinesq flows, multiple instability modes are still detected. By reducing the system of full governing Navier-Stokes equations to a dynamical system of coupled Landau-type disturbance amplitude equations we compute a comprehensive parametric map of various shear-driven instabilities observed in a representative moderately non-Boussinesq regime. Subsequently, we analyze nonlinear interaction of unstable modes and reveal physical reasons for their appearance.

DOI: 10.1103/PhysRevE.81.026301 PACS number(s): 47.20.Bp, 47.20.Ky, 47.15.Rq, 47.55.pb

I. INTRODUCTION

Natural or mixed convection in a tall differentially heated channel is one of the most studied classical convection problems. The literature available on this subject is extensive: its volume is second only to that of the Rayleigh-Bénard configuration. A review of related early studies can be found, for example, in [1,2] and will not be repeated here for the sake of keeping the paper balanced and brief. Despite the fact that this problem has been the subject of active research over the last half a century, the number of authors dealing with its various modifications keeps increasing every year, see, for example, [3,4] for a review of more recent research. This popularity is due to the large number of engineering and industrial applications where mixed convection flows occur, as well as the relative simplicity of analysis which takes advantage of straightforward geometry. Typically, Boussinesq approximation for nonisothermal Navier-Stokes equations is used (e.g., [5]). However the accuracy of the Boussinesq treatment, where all fluid's transport properties are assumed to be constant, deteriorates rapidly in strongly nonisothermal flows [1] such as those existing, for example, in thermal insulation systems or chemical vapor deposition reactors [6,7]. This is due to the essential fluid properties dependence on the temperature which is ignored under the Boussinesq assumption. Accounting for such a dependence using experimentally established constitutive laws renders the governing equations strongly nonlinear and thus difficult for analytical studies. This prompted various recent authors to employ purely numerical investigation of high-temperature flows, see, for example, [8], and references therein. Despite the sophisticated nature of such computations, typically, they can only provide quantitative flow information for a (small) number of points in the governing parameter space. Thus they cannot serve as a tool for the systematic identification of qualitative physical features which drastically distinguish realistic non-Boussinesq flows from their oversimplified Boussinesq counterparts. Therefore, here we employ an asymptotic analysis and a dynamical system approach to classify various patterns arising in essentially nonisothermal mixed convection.

A comprehensive study of flow pattern selection and the subsequent nonlinear interaction between them in strongly non-Boussinesq natural convection of air in a tall vertical enclosure was previously undertaken in [9,10]. It was found that at large temperature differences (above 300 K) across the flow domain, emerging flow patterns resulted from an interplay between the shear- and buoyancy-driven instability mechanisms. This is in contrast to classical low-temperature regimes where parallel convection flow becomes unstable due to the flow shear alone. The influence of the pressure gradient applied along a tall vertical channel was subsequently investigated under non-Boussinesq conditions in [11]. It was found that the physical nature of flow instability in both Boussinesq and strongly non-Boussinesq mixed convection regimes remains similar to that found for natural convection flows. However, a different physical effect was detected for moderately non-Boussinesq flows (with the temperature difference in the range of 150–250 K): it was reported that, similar to a strongly non-Boussinesq case, the flow instability in these condition is caused by two competing instability modes both of which however have the same physical (shear-driven) nature as the instability observed in the Boussinesq limit. The goal of the current work is to identify the physical reasons for the transition between these shear-driven instabilities as they have not been pinpointed to date.

In Sec. II, we use a Low-Mach-Number approximation of full Navier-Stokes equations [12], complemented by constitutive laws describing the realistic fluid (air) properties variations, to formulate a moderately non-Boussinesq mixed convection problem. Subsequently, in Sec. III, we present the results of a weakly nonlinear stability study which shows that even in moderately nonisothermal regimes characterized by the temperature variation on the order of 100 K the flow of a common fluid, such as air, reveals a very rich behavior

*ssuslov@swin.edu.au

with fine transitions between various patterns. The appearance of these patterns sensitively depends on flow parameters. A direct link between the governing physical parameters and model dynamical system coefficients is established and discussed in Sec. III also. Finally, the physical nature of the arising patterns and their interactions is discussed in Sec. IV.

II. PROBLEM FORMULATION

Consider a fluid flow confined by two isothermal vertical plates separated by a gap of width H and maintained at different temperatures T_h and T_c, $T_h > T_c$. The driving pressure gradient Π_y is applied along the channel (in the y direction). The fluid (air) has the average (reference) temperature $T_r = (T_h + T_c)/2 = 300$ K, density ρ, dynamic viscosity μ, thermal conductivity k, and specific heat c_p, all nondimensionalized using their values at T_r and varying with nondimensional temperature T according to the ideal gas law and Sutherland formulas [13]

$$\rho T = 1, \quad c_p = 1, \tag{1}$$

$$\mu = T^{3/2}\frac{1.368}{T + 0.368}, \quad k = T^{3/2}\frac{1.648}{T + 0.648}. \tag{2}$$

As discussed in [2], such a flow is accurately described by the Low-Mach-Number equations [12]. which, upon nondimensionalization using the gap width H, viscous speed $u_r = \mu_r/(\rho_r H)$, characteristic time $t_r = H/u_r$ and characteristic pressure $\Pi_r = \rho_r u_r^2$, are given as

$$\frac{\partial \rho}{\partial t} + \frac{\partial \rho u_i}{\partial x_i} = 0, \tag{3}$$

$$\frac{\partial \rho u_i}{\partial t} + \frac{\partial \rho u_i u_j}{\partial x_j} = -\frac{\partial \Pi}{\partial x_i} + \frac{\mathrm{Gr}}{2\epsilon}(\rho - 1)n_i + \frac{\partial \tau_{ij}}{\partial x_j}, \tag{4}$$

$$\rho c_p\left(\frac{\partial T}{\partial t} + u_j\frac{\partial T}{\partial x_j}\right) = \frac{1}{\mathrm{Pr}}\frac{\partial}{\partial x_j}\left(k\frac{\partial T}{\partial x_j}\right), \tag{5}$$

where $x_i = (x, y)$, $u_i = (u, v)$, $n_i = (0, -1)$,

$$\tau_{ij} = \mu\left(\frac{\partial u_i}{\partial x_j} + \frac{\partial u_j}{\partial x_i} - \frac{2}{3}\delta_{ij}\frac{\partial u_k}{\partial x_k}\right),$$

δ_{ij} is Kronecker delta and summation convention is used. System of equations (1)–(5) is subject to the no-slip/no-penetration velocity conditions and isothermal boundary conditions $T = 1 \pm \epsilon$ at $x = 0$ and $x = 1$, respectively. The Grashof, Reynolds, and Prandtl numbers and nondimensional temperature difference between the walls governing the problem are defined using the reference values (denoted by subscript r) as

$$\mathrm{Gr} = \frac{\rho_r^2 g(T_h - T_c)H^3}{\mu_r^2 T_r}, \quad \mathrm{Re} = -\frac{\rho_r H^3}{12\mu_r^2}\Pi_y,$$

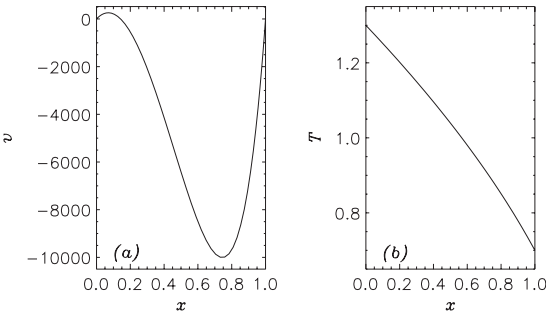

FIG. 1. (a) Basic flow velocity and (b) temperature profiles at the codimension-2 point $(\mathrm{Re}_*, \mathrm{Gr}_*) = (-5179.405, 526921.8)$.

$$\mathrm{Pr} = \frac{\mu_r c_{pr}}{k_r} = 0.71, \quad \epsilon = \frac{T_h - T_c}{2T_r}.$$

They characterize the buoyancy force, the strength of the applied pressure gradient entering the mathematical formulation through inlet/outlet boundary conditions, the ratio of viscous and thermal properties of the fluid (air), and the deviation from Boussinesq model (which can be recovered by considering the limit $\epsilon \to 0$ in the governing equations, see [2]), respectively. Here we investigate in detail flow patterns arising in the representative moderately non-Boussinesq mixed convection regime in the parametric vicinity of $(\mathrm{Re}_*, \mathrm{Gr}_*, \epsilon) = (-5179.405, 526921.8, 0.3)$. The reason for choosing these values will become apparent below. The steady y-independent parallel basic flow profiles satisfying Eqs. (1)–(5) are shown in Fig. 1: downward (as emphasized by the negative value of Reynolds number) flow caused by the applied pressure gradient is opposed by the buoyancy force near the hot wall. The temperature difference between the walls in this regime is 180 K and the fluid thermal diffusivity vary significantly across the channel (up to 15%) so that the temperature deviates from a classical Boussinesq linear profile.

Comprehensive linear stability analysis of such a flow undertaken in [2] revealed a number of remarkable features seen in Fig. 2. First, in contrast to results obtained in low-temperature Boussinesq limit $\epsilon \to 0$ the marginal stability curve Gr(Re) obtained for $\epsilon = 0.3$ has a kink singularity at this set of parameters. Second, both critical wave number α

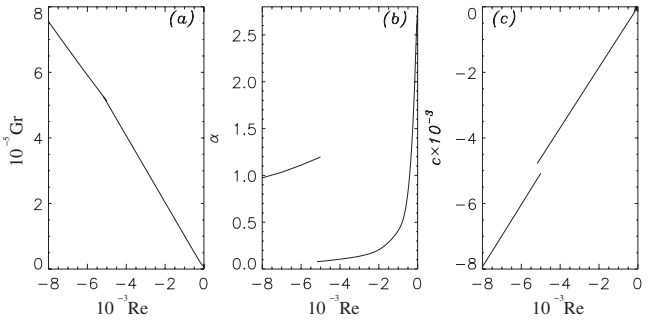

FIG. 2. Linear stability diagram for mixed convection in a vertical channel for $\epsilon = 0.3$: (a) stability boundary (basic parallel flow is unstable above the solid line); (b) neutral disturbance wavenumber and (c) wavespeed.

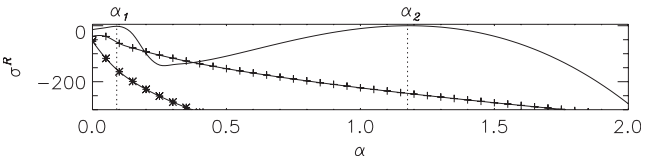

FIG. 3. Leading disturbance amplification rates at the codimension-2 point in non-Boussinesq mixed convection. Symbols mark the amplification rates of the first two decaying modes.

and critical disturbance wave speed c are discontinuous at this point. This situation was previously identified in [2] as a switch between two distinct shear-driven instabilities, but no further analysis has been developed to date. Given that such a phenomenon has never been detected in Boussinesq flows in a similar geometry, investigating the non-Boussinesq flow patterns arising near the "switch" point is a valuable exercise that sheds light on qualitatively different physical mechanisms activated in common fluids by large temperature gradients. In the next section, we present a systematic pattern classification study using a model dynamical system consistently derived from full governing Eqs. (1)–(5).

III. MODEL DYNAMICAL SYSTEM AND CODIMENSION-2 UNFOLDINGS

In this section, we report the major analytical results obtained using linear and weakly nonlinear analyses of the physical problem under consideration. To keep focus on major findings, we intentionally leave routine and somewhat lengthy derivation details outside of the paper. The interested reader can find these details along with the information on numerical implementation in references provided below.

Linear stability analysis of basic flow solutions depicted in Fig. 1 shows that infinitesimal disturbance quantities can be found in a normal form proportional to $\exp(\sigma t+i\alpha y)$, $\sigma=\sigma^R+i\sigma^I$. The leading real disturbance amplification rate curve $\sigma^R(\alpha)$ obtained for $(\mathrm{Re}_*,\mathrm{Gr}_*)$ using the numerical procedure described in detail in [2] is shown by the plain solid line in Fig. 3. It has a peculiar shape: it possesses two zero maxima at wavenumbers $\alpha_1=0.0795$ and $\alpha_2=1.1804$. This is the so-called codimension-2 point. Depending on the values of physical parameters in the vicinity of $(\mathrm{Re}_*,\mathrm{Gr}_*)$, left or/and right maxima cross the zero level. The resulting flow pattern depends on a nonlinear interaction between two disturbance wave envelopes centered at wavenumbers α_1 and α_2 shown by vertical dotted lines in Fig. 3. Both disturbance wave envelopes belong to the same branch of the problem dispersion relation. Hence, they have the same physical nature, namely, the shear which is maximal near the inflection point of the basic flow velocity profile. This is consistent with conclusions made in [2], but there it was overlooked that the instability is caused by the same shear mode (switching the wavenumber) rather than by two distinct modes. The asymptotic behavior of the system is determined by relatively narrow neighborhoods of α_1 and α_2 for which the temporal amplification rate σ^R is positive. Since α_1 and α_2 are well separated from each other, in the context of further derivation, we consider the corresponding wave envelopes as independent objects subject to weakly nonlinear interaction. Systematic disturbance amplitude expansion about the basic flow solution detailed in [9,11] and adapted to the codimension-2 analysis in [10] is truncated to the third order in amplitudes $A_1(t)$ and $A_2(t)$ which correspond to the disturbances with wavenumbers α_1 and α_2, respectively. The expansion then reads [22]

$$\begin{aligned}\mathbf{w} = \mathbf{w}_{000} &+ |A_1|^2\mathbf{w}_{200}^{(1)} + |A_2|^2\mathbf{w}_{200}^{(2)} + \{[A_1(\mathbf{w}_{110} + |A_1|^2\mathbf{w}_{310}^{(1)} \\ &+ |A_2|^2\mathbf{w}_{310}^{(2)})E_1 + A_1^2\mathbf{w}_{220}E_1^2 + A_1A_2^*\mathbf{w}_{21-1}E_1E_2^{-1} + A_2(\mathbf{w}_{101} \\ &+ |A_1|^2\mathbf{w}_{301}^{(1)} + |A_2|^2\mathbf{w}_{301}^{(2)})E_2 + A_2^2\mathbf{w}_{202}E_2^2 + A_1A_2\mathbf{w}_{211}E_1E_2] \\ &+ \text{c.c.}\}, \end{aligned} \tag{6}$$

where $\mathbf{w}=(u,v,T,\Pi)^T$, the first index corresponds to the order of amplitude, the second and the third to the powers of $E_1=\exp(i\alpha_1 y)$ and $E_2=\exp(i\alpha_2 y)$. The asterisk and c.c. denote complex conjugate. Vectors $\mathbf{w}_{110}$ and $\mathbf{w}_{101}$ are eigenvectors of the linearized problem which we normalize so that $\max_{x\in[0,1]}|v_{110}|=\max_{x\in[0,1]}|v_{101}|=\max_{x\in[0,1]}|v_{000}|$. Such a normalization ensures that amplitudes A_1 and A_2 measure directly the size of disturbances relative to the basic flow velocity. In order for Eq. (6) to satisfy Eqs. (1)–(5) in the absence of resonances (as confirmed below) the evolution of disturbance amplitudes should be governed by a system of coupled Landau equations

$$\frac{da_j}{dt} = a_j(\sigma_j^R + K_{j1}^R a_1^2 + K_{j2}^R a_2^2), \tag{7}$$

$$\frac{d\theta_j}{dt} = \sigma_j^I + K_{j1}^I a_1^2 + K_{j2}^I a_2^2, \tag{8}$$

where $A_j=|A_j|\exp(i\theta_j)=a_j\exp(i\theta_j)$ and $\sigma_j=\sigma_j^R+i\sigma_j^I$ are eigenvalues of the linearized problem. The complex Landau coefficients $K_{jk}=K_{jk}^R+iK_{jk}^I$, $j,k=1,2$, are determined by the orthogonality conditions [9]

$$\begin{aligned} &K_{11}:\langle\mathbf{w}_{310}^{(1)},\mathbf{w}_{110}\rangle=0, \quad K_{12}:\langle\mathbf{w}_{310}^{(2)},\mathbf{w}_{110}\rangle=0, \\ &K_{21}:\langle\mathbf{w}_{301}^{(1)},\mathbf{w}_{101}\rangle=0, \quad K_{22}:\langle\mathbf{w}_{301}^{(2)},\mathbf{w}_{101}\rangle=0, \end{aligned} \tag{9}$$

where the angle brackets denote an inner product. These conditions ensure that any new hierarchically added higher order terms are orthogonal to terms with similar y periodicity, which are already present in the expansion. As shown in [9], this amplitude normalization approach reduces to a conventional solvability condition at the bifurcation point. At the same time, when the parametric distance from the bifurcation point is finite, this method allows us to project the solution of the full problem onto a space spanned by eigenfunctions from the linearized problem (computed at a given set of parameters rather than at a bifurcation point) in such a way that the desired physical characteristics of the solution (e.g., the kinetic energy [14] or heat transfer rate [15] of a disturbed flow) are captured most efficiently by the leading expansion terms. Which exactly flow feature is emphasized in the expansion is determined by the choice of the (weighted) inner product [14]. Since in this study we do not focus on any specific flow characteristics but are interested in general clas-

TABLE I. Numerical values for model coefficients for representative points in Fig. 4.

Point	Re	Gr	σ_1	σ_2	$K_{11}\times 10^{-4}$	$K_{12}\times 10^{-7}$	$K_{21}\times 10^{-5}$	$K_{22}\times 10^{-7}$
(1)	Re_*	Gr_*	$0+379.9i$	$0+6197.0i$	$-1.203+0.689i$	$-0.590+1.050i$	$8.058+1.613i$	$-0.637-1.230i$
(2)	Re_*	525000	$-0.574+377.6i$	$-4.802+6159.8i$	$-1.037+0.376i$	$-1.933+4.392i$	$6.023+3.621i$	$-10.26+50.46i$
(3)	−5100	519000	$0.047+380.1i$	$-4.396+6111.2i$	$-1.214+0.703i$	$-0.815+2.144i$	$5.799+3.333i$	$-3.685+15.78i$
(4)	−5100	520000	$0.352+381.4i$	$-1.906+6130.6i$	$-1.279+0.817i$	$-0.415+1.006i$	$6.794+2.462i$	$-0.533+1.976i$
(5)	−5100	521000	$0.657+382.6i$	$0.588+6149.3i$	$-1.336+0.912i$	$-0.603+0.992i$	$7.486+1.280i$	$-0.621+1.121i$
(6)	Re_*	530000	$0.924+383.7i$	$7.714+6255.4i$	$-1.381+0.982i$	$-0.936+0.649i$	$7.916-2.528i$	$-0.586-0.875i$
(7)	−5250	533000	$-0.337+378.5i$	$1.392+6253.7i$	$-1.112+0.519i$	$-0.717+1.032i$	$8.890+0.914i$	$-0.645-1.095i$

sification of flow patterns near the double-Hopf bifurcation in moderately non-Boussinesq convection all results reported in this paper are produced using a standard inner product for complex vectors: $\langle \mathbf{q},\mathbf{r}\rangle=\mathbf{q}^{*T}\cdot\mathbf{r}$.

Note that all coefficients in equations (7) and (8) depend on physical governing parameters. Due to this fact the analysis of the codimension-2 dynamics is a nontrivial and numerically involved task. Yet the computational time required to obtain a complete and accurate parametric map corresponding to various physical solutions is several orders of magnitude smaller than that of direct numerical simulation. This justifies the current analytical effort. The implemented computational procedure first identifies the wavenumbers α_1 and α_2 of the fastest growing disturbances for each parameter pair (Re, Gr) in the vicinity of $(\mathrm{Re}_*,\mathrm{Gr}_*)$. Once this is done the hierarchy of differential equations for $\mathbf{w}_{ijk}$ arising at various orders of disturbance amplitude is solved. Subsequently, the orthogonality conditions (9) are applied to determine the Landau coefficients defining equations (7) and (8), which is analyzed next. The numerical values for model coefficients for representative parameter values near the codimension-2 point are given in Table I.

In order to analyze models (7) and (8), we follow the relevant discussions found in two popular texts on dynamical systems [16,17]. First, we consider two amplitude Eqs. (7) since they are completely decoupled from the phase Eqs. (8). We apply transformations

$$r_1=a_1\sqrt{|K_{11}^R|},\quad r_2=a_2\sqrt{|K_{22}^R|},$$

$$\mu_1=-\sigma_1^R,\quad \mu_2=-\sigma_2^R,$$

$$b=-\frac{K_{12}^R}{|K_{22}^R|},\quad c=-\frac{K_{21}^R}{|K_{11}^R|},\quad d=-\frac{K_{22}^R}{|K_{22}^R|},\quad t\to -t$$

suggested in [16] to reduce Eqs. (7) to the canonical form

$$\dot r_1=r_1(\mu_1+r_1^2+br_2^2),\quad \dot r_2=r_2(\mu_2+cr_1^2+dr_2^2). \tag{10}$$

As seen from Table I, both K_{11}^R and K_{22}^R are negative in the vicinity of $(\mathrm{Re}_*,\mathrm{Gr}_*)$ so that both modes bifurcate supercritically. Therefore, the third-order amplitude expansion (6) is sufficient to estimate the saturation disturbance amplitudes. Numerical evaluation of the system coefficients at $(\mathrm{Re}_*,\mathrm{Gr}_*)$ results in $b=0.925$, $c=-67.340$, $d=1$, $\mu_1=\mu_2=0$, which corresponds to Type 2a case II of the fixed point with three invariant lines $(r_1=0,\ r_2=0,\ r_2=\sqrt{(1-c)/(d-b)})$ according to the classification given in Tables 7.5.1 and 7.5.2 in [16]. In order to unfold this bifurcation, note that the four types of equilibria (r_{1e},r_{2e}) are possible in system (10): (a) linearly stable basic flow, (0,0); (b), and c) individually bifurcating modes $(\sqrt{-\mu_1},0)$ and $(0,\sqrt{-\mu_2/d})$; and d) interacting modes $(\sqrt{(b\mu_2-d\mu_1)/(d-bc)},\sqrt{(c\mu_1-\mu_2)/(d-bc)})$. Stability of the above fixed points is determined by the eigenvalues $\lambda_{1,2}$ of a problem obtained by linearizing Eqs. (10) about the equilibrium (r_{1e},r_{2e}). The stability conditions then is $\lambda_{1,2}^R>0$ (because of the time reversion), where

$$\lambda_{1,2}=\frac{C_{11}+C_{22}\pm\sqrt{16bcr_{1e}^2r_{2e}^2+(C_{11}-C_{22})^2}}{2}, \tag{11}$$

$$C_{11}=\mu_1+3r_{1e}^2+br_{2e}^2,\quad C_{22}=\mu_2+3dr_{2e}^2+cr_{1e}^2.$$

More specifically, for $d=1$ equilibria (a)–(c) are stable if, respectively: (a) $\mu_1,\mu_2>0$; (b) $\mu_2>c\mu_1$; (c) $\mu_1>b\mu_2$; equilibrium (d) is always stable if it exists. Consequently, unfoldings of the codimension-2 point are determined by lines $\mu_1=0$, $\mu_2=0$, $\mu_2=c\mu_1$, and $\mu_1=b\mu_2$. All topologically distinct amplitude flow diagrams near the considered codimension-2 point are presented in Fig. 4. Straight lines $a_1=0$, $a_2=0$ and $a_2=a_1\sqrt{(K_{11}^R-K_{21}^R)/(K_{22}^R-K_{12}^R)}\approx 1.319a_1$ in plot (1) are the invariant lines at the codimension-2 point $(\mathrm{Re}_*,\mathrm{Gr}_*)$. The third of these lines is algebraically attractive so that the distance between it and the trajectories decreases asymptotically as $t^{-3/2}$ while the evolution along the invariant line toward the origin is $a_1\sim a_2\sim t^{-1/2}$. Plots (2)–(7) show all possible unfoldings of a fixed point for case II in [16]. The middle plot in Fig. 4 relates unfoldings to the physical parameter space for non-Boussinesq mixed convection.

Note that unfoldings shown in Fig. 4 are not discussed in [16], but given in ([17], Chapter 8.6) [23] as case III of "Simple" Hopf-Hopf bifurcation. According to Fig. 8.25 in [17], the amplitude flow diagrams (2)–(7) shown in Fig. 4 correspond to phase portraits ①, ②, ⑥, ⑤, ⑬, and ⑪ in Fig. 8.26 in [17], respectively. Diagrams (4) and (6), however, appear different from their counterparts ⑥ and ⑬ in [17]. More specifically, phase portrait ⑥ in [17] indicates the presence of a stable node, while the computed amplitude flow diagram (4) contains a stable focus. The eigenvalues (11) in this case can be written as

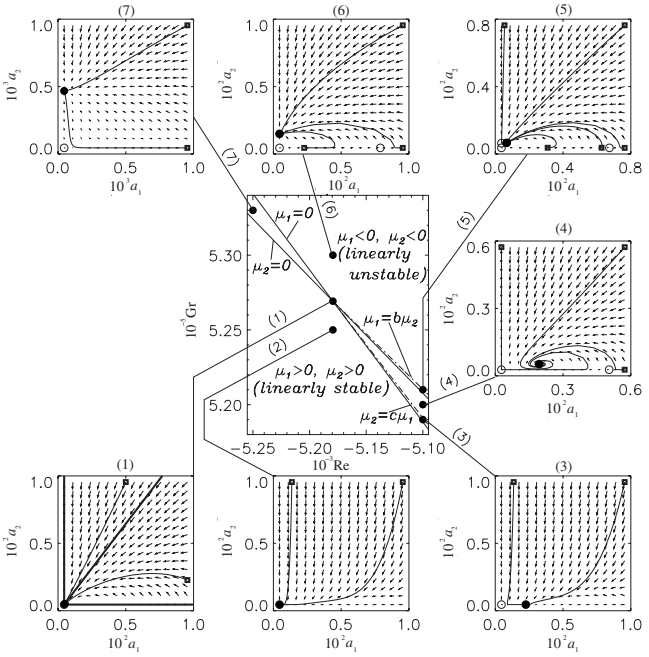

FIG. 4. Amplitude flow diagrams and trajectories near the codimension-2 point. Squares and empty and filled circles represent initial conditions and unstable and stable equilibria, respectively.

$$\lambda_{1,2} = r_{1e}^2 + r_{2e}^2 \pm \sqrt{(r_{1e}^2 - r_{2e}^2)^2 + 4bcr_{1e}^2 r_{2e}^2}, \qquad (12)$$

where $bc<0$. Thus, depending on the values of the equilibrium amplitudes $r_{1,2e}$ and coefficients b and c the expression under the square root could be either positive or negative. The former would correspond to phase portrait ⑥ while the latter results in amplitude diagram (4). However, according to the definitions given in [17], both situations are topologically equivalent.

The discrepancy between the amplitude flow diagram (6) in Fig. 4 and the phase portrait ⑬ given for this case in [17] is however topologically essential. Indeed it is suggested in [17] that a stable fixed point of type (d) identified previously in this section should exist. However, a simple analysis shows that in region (6) of the middle plot in Fig. 4, the expression $(b\mu_2 - d\mu_1)/(d-bc)$ is always negative and thus cannot represent a square of a disturbance amplitude. This means that fixed point of type (d) cannot be present in this parametric region and the amplitude flow diagram (6) [24] should be considered as the true representation of amplitude dynamics.

In order to complete the analysis, the phase evolution given by Eqs. (8) has to be considered and in particular the possibility of phase locking and resonances has to be examined. The phase locking condition is

$$\sigma_1^I - \sigma_2^I + (K_{11}^I - K_{21}^I)a_1^2 + (K_{12}^I - K_{22}^I)a_2^2 = 0. \qquad (13)$$

Differentiating this equation with respect to time and using (7) after some algebra, we conclude that (13) may be satisfied only if both amplitudes are constant, i.e., at the stable mixed fixed points $a_{1e}a_{2e} \neq 0$ existing in between the dash-dotted lines in Fig. 4 [see plots (4) and (5) for the flow topography]. Condition (13) then becomes

$$\frac{(K_{11}^I - K_{21}^I)(\sigma_2^R K_{12}^R - \sigma_1^R K_{22}^R) + (K_{12}^I - K_{22}^I)(\sigma_1^R K_{21}^R - \sigma_2^R K_{11}^R)}{K_{11}^R K_{22}^R - K_{12}^R K_{21}^R} = \sigma_2^I - \sigma_1^I,$$

but it is not satisfied anywhere in Fig. 4. Finally, the ratios σ_2^I/σ_1^I and α_2/α_1 remain between 16 and 17 and 14 and 15, respectively, for all points in Fig. 4. Hence, no strong resonances occur and the performed analysis based on the third-order expansion (6), accounting for the evolution of amplitude modulus only, is sufficient.

IV. PHYSICAL INTERPRETATION OF DYNAMICAL SYSTEM RESULTS

Next, we relate the results reported in the previous section to the physical flow under consideration. It has been mentioned in Sec. II that the flow between the plates is determined by two competing mechanisms: the buoyancy force and the pressure gradient applied along the channel. The parallel basic flow becomes unstable due to the action of shear, which is maximum near the inflection point of the basic flow velocity profile, see Fig. 1(a). This is indeed confirmed by plots (a) and (b) in Fig. 5 where the weakly nonlinear disturbance fields given by Eq. (6) are reconstructed: the disturbance structures are most profound in the middle of the channel near the inflection point. Since the inflection point appears due to the action of the buoyancy force characterized by Grashof number it is only present if the ratio $\mathrm{Gr}/|\mathrm{Re}|$ is sufficiently large. For this reason the critical Grashof number increases rapidly with $|\mathrm{Re}|$ as seen from Fig. 2(a). At the nearly zero values of $|\mathrm{Re}|$ (small pressure gradient), the instability is characterized by almost stationary secondary rolls [which have nearly zero wavespeed, see Fig. 2(c)] with the wavelength $\lambda = 2\pi H/\alpha \approx 2.3H$ [Fig. 2(b)]. As the driving pressure gradient increases, these rolls start drifting downward with the primary flow and elongate. Thus, the pressure gradient has a stretching effect on the flow instability structures. This effect is evident from comparing plots (a) and (b) in Fig. 5. Shear-stretching of instability cells continues until the size of the rolls becomes so large that they start blocking the primary flow strongly. At the codimension-2 point, these large aspect ratio instability rolls with $\lambda \approx 79H$ break into smaller ones with $\lambda \approx 5.3H$ which drift with a larger wave speed [see Fig. 2(c)] so that their "blocking" effect is less profound. Note that such a transition between the flow patterns is not because of the secondary instability of the large aspect ratio rolls, but rather due to a competition between the two distinct flow structures one of which drains the energy from another. This competition is illustrated in Fig. 4. For any fixed $\mathrm{Re} > \mathrm{Re}_*$, the basic flow [plot (2)] first becomes unstable due to the long wave disturbances [plot (3)], which trigger their own distortion at the slightly higher values of Gr [plot (4)]. This distortion is supported by draining the energy from the large instability rolls to finer structures (because the coupling coefficients $K_{21}^R > 0$ and $K_{12}^R < 0$) via nonlinear interaction. At even higher values of Gr the smaller rolls become self-supporting by draining the energy from the basic flow [σ_2 becomes positive in plot (5)] and eventually destroy

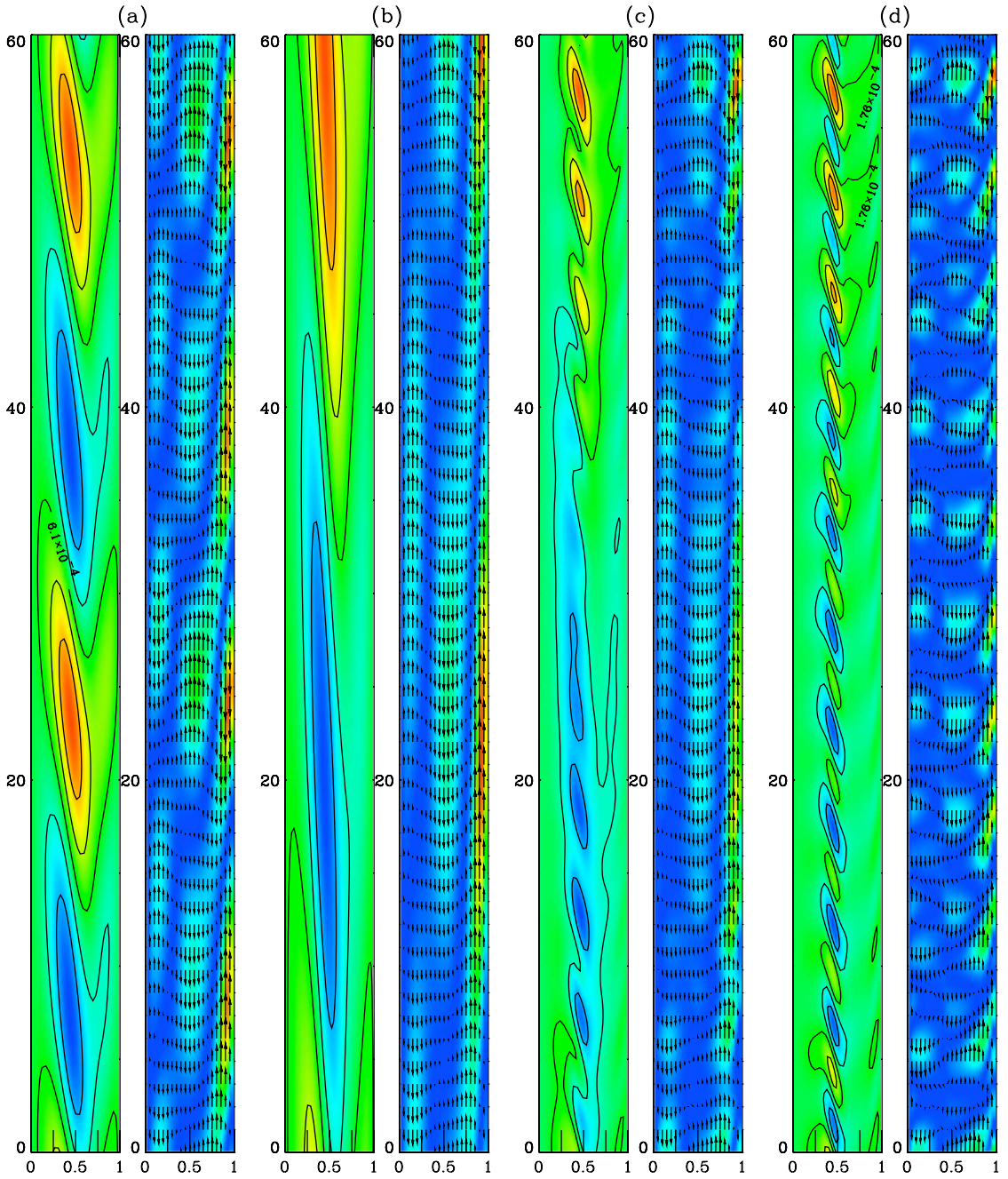

FIG. 5. (Color online) Selected disturbance thermal (left) and velocity (right) fields near the codimension-2 point at various values of (Re, Gr): (a) (−2000,204000), (b) (−5100,519000), (c) (−5100,520000), and (d) (−5100,521000). Gray shades (color) visualize the temperature (left plots) and kinetic energy (right plots) fields. Fields (b)–(d) correspond to plots (3)–(5) in Fig. 4, respectively.

the large rolls completely [plot (6)]. This sequence of events is illustrated by the instantaneous disturbance fields shown in plots (b)–(d) in Fig. 5. For $\mathrm{Re} < \mathrm{Re}_*$, the small roll instability structures always dominate and large rolls cannot be observed [plots (2), (6), and (7) in Fig. 4].

V. CONCLUSIONS

It is demonstrated that consistent accounting of realistic fluid property variations in strongly nonisothermal mixed convection flows reveals a rich variety of possible flow patterns even in the simplest geometric configurations. These possible patterns result from an intricate interplay between various nonlinearities brought about by realistic constitutive laws. Such flows cannot be described using a standard Boussinesq model which assumes constant fluid properties or, at best, their linear variation with temperature. In fact, complex multimode instability analyzed in this paper disappears completely if conventional Boussinesq equations are inconsistently used to model the flow. Using the Low–Mach-Number approximation of Navier-Stokes equations instead, we found that the shear-driven instability detected in moder-

ately non-Boussinesq mixed convection is structurally different from that observed in the Boussinesq limit, and that the physical mechanism of the studied instability is qualitatively different from that of its high-temperature counterpart investigated previously. The major technical result of the current study is a detailed parametric map of various flow patterns arising near a codimension-2 bifurcation point, which is detected in moderately non-Boussinesq mixed convection flow caused by the competing upward buoyancy force near the heated surface and the applied opposing pressure gradient. Physical reasons for the existence of the observed flow patterns are also discussed.

Finally, we make several brief notes in order to put the findings reported here in a wider context. The fact that fluid properties variations with temperature quantitatively affect flow characteristics is hardly surprising and is widely acknowledged (e.g., [18]). For example, a large body of literature exists which is concerned with the influence of temperature-dependent viscosity on incompressible convection flow parameters (e.g., [19]). However to simplify the analysis many of such studies deal with hypothetical fluids exhibiting strong variation on one property (e.g., viscosity), but not the others (i.e., density or thermal conductivity) (e.g., [20]). Inevitably, the results obtained for such artificial fluids are not quantitatively fit for realistic flows. In contrast, in the current work a flow of a very common fluid (air) was investigated and all its properties were consistently accounted for. The other noteworthy point is that even when all fluid properties variations are carefully considered, the deviation of flow patterns from a nearly isothermal case may be of an incremental rather than qualitatively new nature. For example, a comprehensive study of non-Boussinesq mixed convection flow of air in a horizontal channel undertaken in [21] did not reveal any features qualitatively different from those found in constant fluid properties flows. Yet, similar flows in a vertical channel detailed here do possess qualitatively distinct features. Therefore, we conclude that the bifurcations reported here are the consequences not only of fluid property variations, but also of their interplay with external factors such as the gravity orientation relative to the primary temperature gradient.

[1] D. D. Gray and A. Giorgini, Int. J. Heat Mass Transfer **19**, 545 (1976).
[2] S. A. Suslov and S. Paolucci, J. Fluid Mech. **302**, 91 (1995).
[3] T.-F. Lin, Int. J. Heat Fluid Flow **24**, 299 (2003).
[4] T. Yilmaz and S. M. Fraser, Int. J. Heat Mass Transfer **50**, 2612 (2007).
[5] J. Mizushima and H. Tanaka, Phys. Fluids **14**, L21 (2002).
[6] G. W. Young, S. I. Hariharan, and R. Carnahan, SIAM J. Appl. Math. **52**, 1509 (1992).
[7] G. Evans and R. Greif, Int. J. Heat Mass Transfer **36**, 2769 (1993).
[8] W.-S. Fu, C.-G. Li, C.-P. Huang, and J.-C. Huang, Int. J. Heat Mass Transfer **52**, 2571 (2009).
[9] S. A. Suslov and S. Paolucci, J. Fluid Mech. **344**, 1 (1997).
[10] S. A. Suslov and S. Paolucci, *Proceedings of the ASME Heat Transfer Division*, edited by M. E. Ulucakli *et al.* (ASME Press, New York, 1997), Vol. 3, pp. 243–250.
[11] S. A. Suslov and S. Paolucci, J. Fluid Mech. **398**, 61 (1999).
[12] S. Paolucci, Sandia National Laboratories Technical Report No. SAND82-8257, 1982 (unpublished).
[13] F. M. White, *Viscous Fluid Flow* (McGraw-Hill, New York, 1974).
[14] S. A. Suslov, Discrete Contin. Dyn. Syst., Ser. S **1**, 165 (2008).
[15] S. A. Suslov, A. A. Bozhko, and G. F. Putin, Proceedings of the 7th International World Conference on Experimental Heat Transfer, Fluid Mechanics and Thermodynamics, Krakow, Poland, 2009, pp. 1257–1264.
[16] J. Guckenheimer and P. J. Holmes, *Nonlinear Oscillations, Dynamical Systems and Bifurcations of Vector Fields* (Springer-Verlag, New York, 1985).
[17] Y. A. Kuznetsov, *Elements of Applied Bifurcation Theory*, 3rd ed. (Springer-Verlag, New York, 2004).
[18] N. G. Kafoussias and E. W. Williams, Acta Mech. **110**, 123 (1995).
[19] J. Severin and H. Herwig, ZAMP **50**, 375 (1999).
[20] O. Hirayama and R. Takaki, Fluid Dyn. Res. **12**, 35 (1993).
[21] O. V. Vasilyev and S. Paolucci, Acta Mech. **112**, 37 (1995).
[22] Strictly speaking, in slightly subcritical regimes, when one of (or both) amplification rate maxima in Fig. 3 attains a negative value one needs to consider the interaction of the mode(s) corresponding to the negative maxima with other decaying modes shown in Fig. 3 by symbols. However, for all computational results presented here, it is found that the difference in σ^R values between different eigenmodes remains finite. Therefore, it is sufficient to retain only the leading modes (solid line) in the expansion (6) to obtain meaningful asymptotic results.
[23] Ref. [17] uses different notations and a canonical form which includes quintic terms in amplitude Eqs. (7). However, these additional terms do not affect the topology of the unfoldings in the considered case.
[24] Incidentally, our diagram (6) is similar to phase portrait ⑫ given in [17] as a part of other unfoldings (not related to the current case). This indicates a possible referencing or typographical error in [17].